ACS OMEGA

http://pubs.acs.org/journal/acsodf

Article

Fe_3O_4 Composite Superparticles with RGD/Magnetic Dual-Targeting Capabilities for the Imaging and Treatment of Non-Small Cell Lung Cancer

Nan Zhao, Qirui Sun, Lening Zhang, Hao Jin, Mengsi Zhang, Shuwei Liu,* and Hua Xin*

Cite This: *ACS Omega* 2023, 8, 7891−7903

Read Online

ACCESS | Metrics & More | Article Recommendations | Supporting Information

ABSTRACT: In clinical practice, the incidence and mortality of non-small cell lung cancer are increasing year by year, which is a serious threat to the health of patients. Once the optimal surgical window is missed, the toxic side effects of chemotherapy have to be confronted. With the rapid development of nanotechnology in recent years, medical science and health have been greatly impacted. Therefore, in this manuscript, we design and prepare chemotherapeutic drug vinorelbine (VRL)-loaded polydopamine (PDA) shell-coated Fe_3O_4 superparticles, and further graft the targeted ligand RGD onto their surface. Because of the introduction of the PDA shell, the toxicity of the prepared Fe_3O_4@PDA/VRL-RGD SPs is greatly reduced. At the same time, due to the existence of Fe_3O_4, the Fe_3O_4@PDA/VRL-RGD SPs also have MRI contrast capability. Under the dual-targeting effect of RGD peptide and external magnetic field, Fe_3O_4@PDA/VRL-RGD SPs can accumulate into tumors effectively. The accumulated superparticles in the tumor sites can not only effectively identify and mark the location and boundary of the tumor under MRI, guideing the application of near-infrared laser, but also release the loaded VRL under the stimulation of the acidic microenvironment of the tumor to play the role of chemotherapy. On further combination with photothermal therapy under laser irradiation, A549 tumors are completely eliminated without recurrence. Our proposed RGD/magnetic field dual-targeting strategy can effectively improve the bioavailability of nanomaterials and contribute to better imaging and therapeutic effects, which has a promising application prospect in the future.

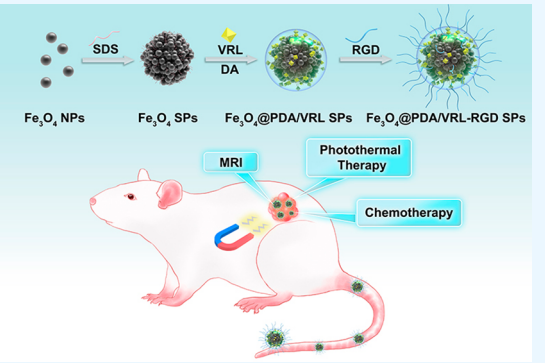

INTRODUCTION

Globally, there were more than 2.2 million new cases of lung cancer in 2020 and nearly 1.8 million deaths from it.[1] Lung cancer is divided into small cell lung cancer and non-small cell lung cancer (NSCLC). The main type of lung cancer is NSCLC, comprising about 85%.[2,3] Surgery is the most effective treatment for NSCLC at stages I−II and some cases at stage III.[4,5] Despite its high malignancy rate, NSCLC usually presents with mild early symptoms. When patients are first seen by a doctor, they may have missed the window of opportunity for surgical treatment, and the 5 year survival rate is low.[6,7] In the clinical treatment of advanced NSCLC, chemotherapy is one of the standard options.[8] However, as a systemic treatment, chemotherapy inevitably damages normal tissues, and the application of chemotherapeutic drugs is severely restricted due to their toxic side effects and inadequate targeting abilities.[9−11] Consequently, reducing the toxic side effects of chemotherapy drugs, improving the drug concentrations in tumor sites, and increasing drug utilization are of great research importance.

Medical science and health have been greatly impacted by the rapid development of nanotechnology in recent years. A growing body of research has also been conducted on nanomedicine and nanocarriers.[12] Various diseases can be diagnosed and treated using multifunctional nanomaterials that take advantage of the unique characteristics of different components of nanomaterials.[13−15] Nanomaterials within a certain size range have a longer circulation time in blood and reach the tumor tissue through a leaky tumor vasculature. As a result of reduced lymphatic drainage, the retention in the tumor increases, which is known as the enhanced permeability and retention (EPR) effect. Many researchers have been working on ways to enhance chemotherapy drug enrichment in solid tumors by loading chemotherapy drugs into nanocarriers and utilizing the EPR effect of nanomaterials.[16−19] However, this method also has some limitations, mainly including three aspects: (1) the problem of enhancing the tumor-targeting ability of nanocarriers; (2) the problem of improving the biological safety of nanocarriers; and (3) the problem of

Received: November 30, 2022
Accepted: February 3, 2023
Published: February 14, 2023

https://doi.org/10.1021/acsomega.2c07647
ACS Omega 2023, 8, 7891−7903

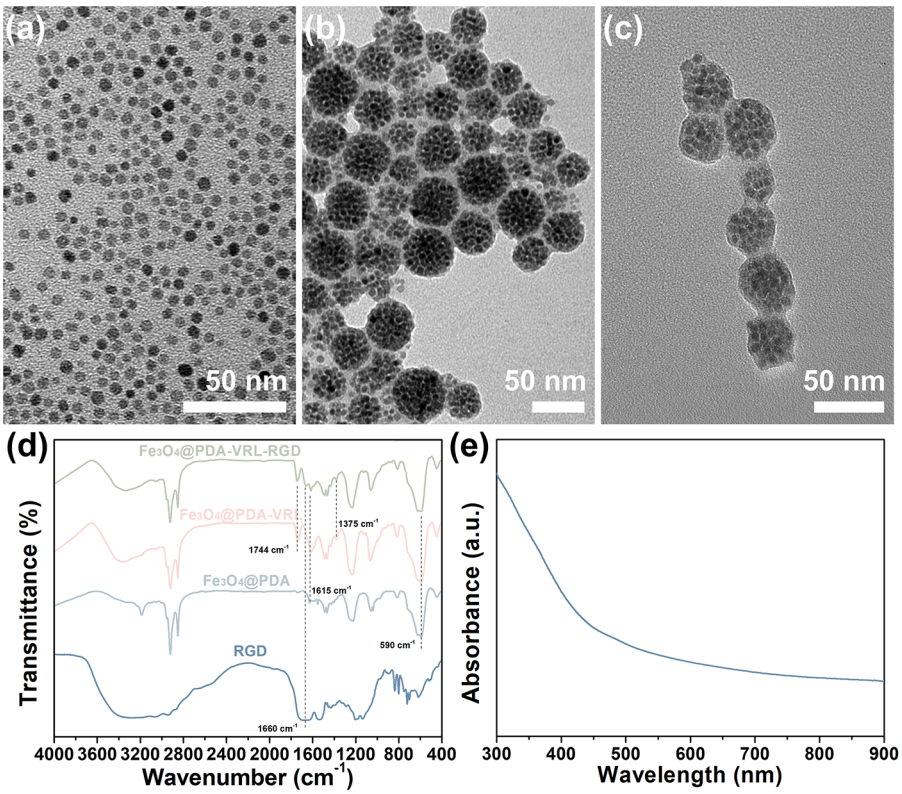

Figure 1. TEM images of Fe_3O_4 NPs (a), Fe_3O_4@PDA/VRL SPs (b), and Fe_3O_4@PDA/VRL-RGD SPs (c). (d) FTIR spectra of Fe_3O_4@PDA SPs, Fe_3O_4@PDA-VRL SPs, Fe_3O_4@PDA/VRL-RGD SPs, and RGD. (e) UV−vis−NIR absorption spectrum of Fe_3O_4@PDA/VRL-RGD SPs.

achieving controlled release of chemotherapy drugs in tumors.[20−22] Therefore, it is of great research significance to construct nanoscaled drug carriers that can target tumor sites, be biosafe, and have tumor microenvironment responsiveness.

Nanocarriers can be grafted with targeting ligands to improve their targeting capabilities.[23,24] It is possible to mediate tumor-targeted therapy using the Arg-Gly-Asp (RGD) peptide, a recognition site for specific integrins expressed by tumor cells and their ligands. Nanocarriers can be modified to improve their tumor-targeting ability by modifying RGD peptides.[25,26] Huang et al. and Zhou et al. reported that, compared with unmodified nanoparticles, the accumulation and content of nanoparticles modified with RGD peptide in lung tumor tissues were significantly increased, which improved the tumor targeting ability of lung cancer.[27,28] Moreover, the targeting ability of nanocarriers can also be affected by changes in the external physical environment.[29,30] By applying a magnetic field to the tumor site, magnetic nanocarriers can be guided to the tumor sites for accurate delivery.[31,32] In recent years, wearable magnetic-targeting devices developed based on magnetic-targeting strategies have achieved rapid development and show potential application in humans.[33] Among magnetic targeting carriers, Fe_3O_4 is the most widely used magnetic building block.[34−36] Given the limited magnetic properties of Fe_3O_4 nanoparticles, the method of constructing tens to hundreds of nanoparticles into superparticles by the self-assembly method can effectively achieve magnetic integration, which can enhance the magnetic targeting ability and improve the MRI imaging effect.[37,38]

The introduction of surfactant is inevitable in the production of Fe_3O_4 SPs, and reducing its toxicity has become a pressing issue.[39] Biological safety can be improved by coating inorganic nanoparticles with polydopamine (PDA).[40] PDA is formed by the polymerization of dopamine monomer under alkaline conditions. Considering that dopamine is a natural neurotransmitter in living organisms, PDA has good biocompatibility.[41,42] In addition, PDA is a good drug carrier due to its high viscosity, presence of catechol, amine, imine, and other functional groups on its surface, as well as its ability to bind with functional ligands via Michael addition and/or Schiff base reactions. Drugs can then be loaded through physical adsorption or chemical coupling.[43] A potentially effective way to control drug release in the tumor microenvironment occurs when PDA disintegrates at a slightly acidic pH.[44] In addition, PDA also has strong near-infrared (NIR) light absorption ability, so it can effectively convert light into heat and play the role of photothermal reagent, with a photothermal conversion efficiency of about 40%.[45,46] When combined with other methods, synergistic therapy is capable of producing better results for the treatment of tumors and preventing the development of drug resistance.[47,48] Therefore, the methods of coating Fe_3O_4 SPs with a chemotherapy drug loaded PDA shell and grafting targeting ligands on the surface of composite superparticles are helpful to enhance the tumor accumulation of composite superparticles under the dual targeting of ligand and magnetic field and to achieve a collaborative treatment of photothermal therapy and chemotherapy for tumors under the guidance of MRI.[49,50]

In this work, we use Fe_3O_4 SPs as the main building block, coat their surface with a chemotherapy drug (vinorelbine (VRL)) loaded PDA shell, graft the PDA shell with targeting ligand RGD peptide, and finally construct the multifunctional Fe_3O_4@PDA/VRL-RGD composite SPs. The loading rate of VRL in composite superparticles is calculated as 15.3%.

https://doi.org/10.1021/acsomega.2c07647
ACS Omega 2023, 8, 7891−7903

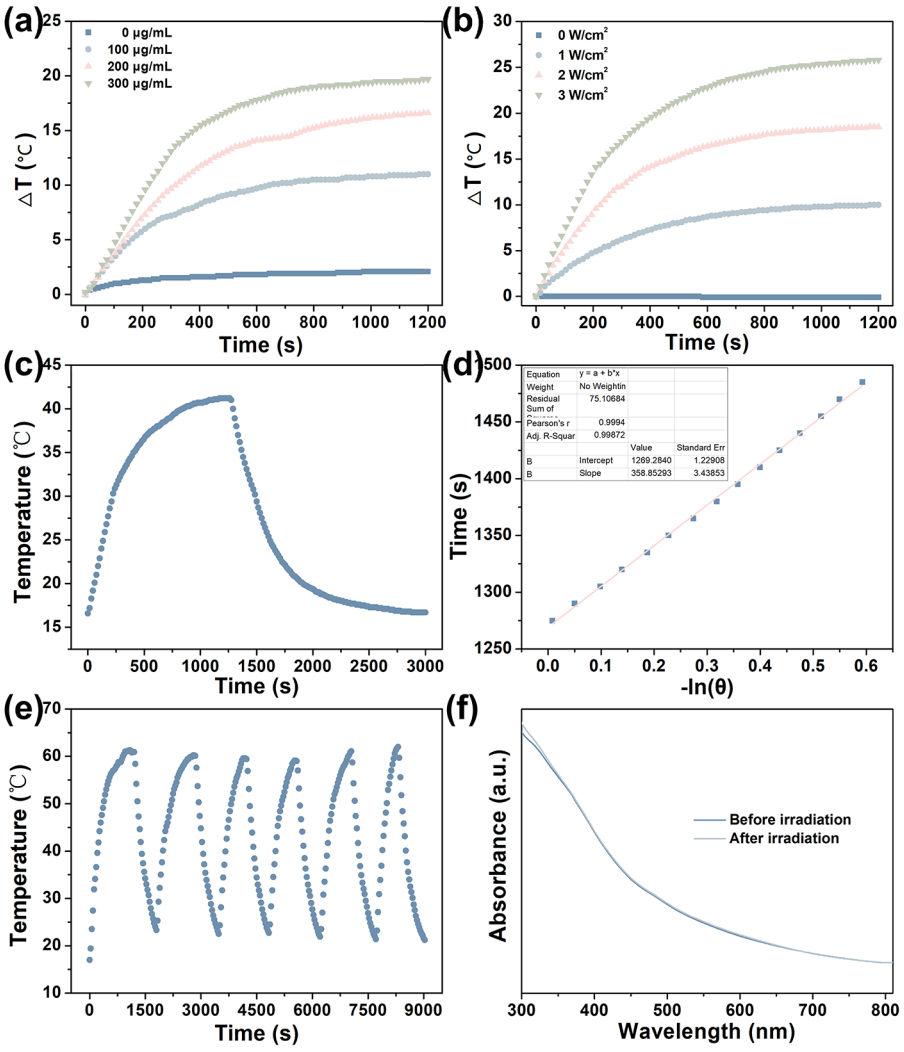

Figure 2. (a) Temperature increments of Fe_3O_4@PDA/VRL-RGD SPs solutions at different concentrations of 0, 100, 200, and 300 μg/mL irradiated by 808 nm laser at 2 W/cm^2. (b) Temperature increments of Fe_3O_4@PDA/VRL-RGD SPs solutions at 200 μg/mL irradiated by 808 nm laser at different power densities of 0, 1, 2, and 3 W/cm^2. (c) Heating−cooling cycle of Fe_3O_4@PDA/VRL-RGD SPs solution at 200 μg/mL under the irradiation of an 808 nm laser at 3 W/cm^2. (d) Linear time versus the negative natural logarithm of driving force temperature during the cooling period. The time constant for heat transfer: τ_s = 358.9 s. The photothermal conversion efficiency is calculated to be η = 46.1%. (e) Six heating−cooling cycles of Fe_3O_4@PDA/VRL-RGD SPs solution at 1000 μg/mL under the irradiation of an 808 nm laser at 3 W/cm^2. (f) UV−vis−NIR absorption spectra of Fe_3O_4@PDA/VRL-RGD SPs before and after the irradiation.

Because of the introduction of the PDA shell, the toxicity of surfactant and chemotherapy drug is greatly reduced. Under the dual-targeting effect of RGD peptide and external magnetic field, Fe_3O_4@PDA/VRL-RGD SPs effectively accumulate into tumors. Fe_3O_4@PDA/VRL-RGD SPs also have MRI imaging ability, so the superparticles accumulated in tumor sites effectively identify the location and boundary of tumors under MRI and guide the application of NIR laser. The heating of tumor tissue under laser irradiation stimulates the release of VRL. At the same time, the VRL loaded in PDA releases in response to a slightly acidic tumor microenvironment, which further improves the effect of chemotherapy. Further combined with the photothermal treatment of composite superparticles under laser irradiation, NSCLC is completely eliminated, and the treatment effect is excellent without recurrence. Our proposed design of dual targeting of tumors by targeting ligands and external magnetic field has broad application prospects in the future.

RESULTS AND DISCUSSION

In this work, a classical thermal decomposition method is first applied to synthesize Fe_3O_4 NPs. As shown in Figure 1a, the size of Fe_3O_4 NPs is uniform, with an average diameter of 5.6 nm under transmission electron microscopy (TEM). Then, toluene is vaporized in an oil-in-water microemulsion containing sodium lauryl sulfate (SDS), and Fe_3O_4 SPs with an average diameter of 41.2 nm are produced. Since dopamine monomers can be adsorbed on the surfaces of negatively charged Fe_3O_4 SPs and have the ability to be oxidized and polymerize under alkaline conditions, the PDA shell is successfully deposited on Fe_3O_4 SPs with an average thickness of 4.2 nm. By introducing the chemotherapeutic drug VRL into the reaction system during the polymerization process, the loading of chemotherapeutic drug in PDA shell can be realized and Fe_3O_4@PDA/VRL SPs are obtained (Figure 1b). In the PDA shell, most of the VRL is inside, while a small amount is absorbed on the surface, and the load of VRL is based on its $\pi-\pi$ stacking with PDA. Finally, RGD is grafted onto the

https://doi.org/10.1021/acsomega.2c07647
ACS Omega 2023, 8, 7891−7903

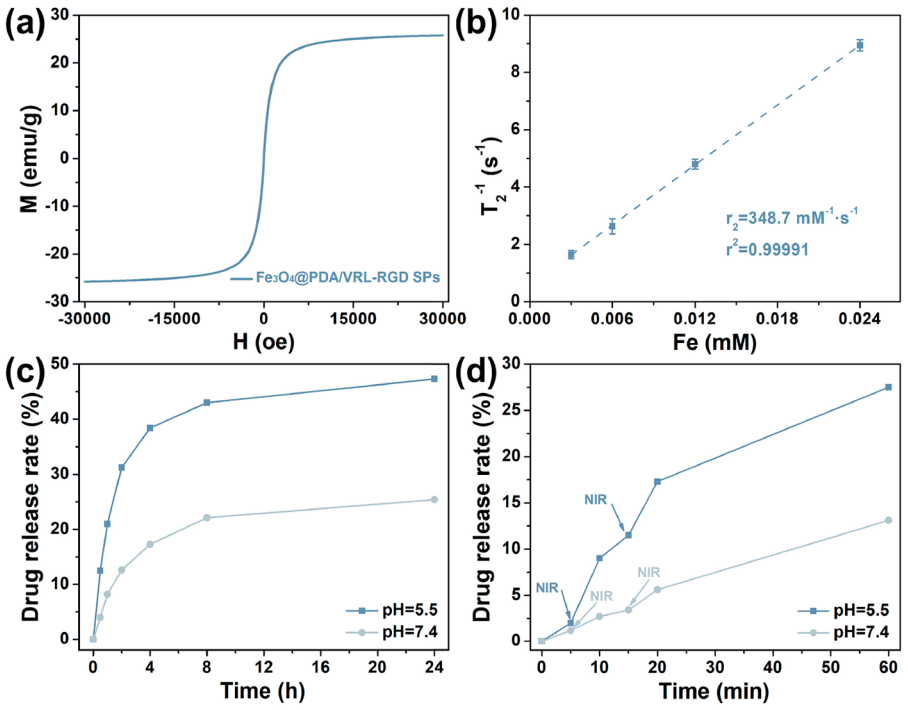

Figure 3. (a) $M-H$ curve of Fe_3O_4@PDA/VRL-RGD SPs under a circulating magnetic field between −30000 and +30000 Oe. (b) Transverse relaxation rate (r_2) of Fe_3O_4@PDA/VRL-RGD SPs. (c) Release rate of VRL from Fe_3O_4@PDA/VRL-RGD SPs overtime in PBS with different pH values of 5.5 and 7.4. (d) Changes of drug release rates after the NIR laser irradiation of 1 W/cm^2.

surface of Fe_3O_4@PDA/VRL SPs to obtain Fe_3O_4@PDA/VRL-RGD SPs with the diameter of 49.6 nm under TEM (Figure 1c). The graft of RGD has little effect on the morphology of Fe_3O_4@PDA/VRL SPs (Figure 1b,c), but it significantly increases the hydrated particle size. The average hydrated particle size of Fe_3O_4@PDA/VRL SPs measured by dynamic light scattering (DLS) is 87.9 ± 0.9 nm, while it increases to 97.5 ± 0.4 nm for Fe_3O_4@PDA/VRL-RGD SPs. The Fourier-transform infrared (FTIR) spectra confirms that the characteristic peaks of RGD (1660 cm^{-1}), Fe_3O_4@PDA SPs (590 cm^{-1}, 1615 cm^{-1}), and Fe_3O_4@PDA/VRL SPs (1375 cm^{-1}, 1744 cm^{-1}) all appear in the characteristic peaks of Fe_3O_4@PDA/VRL-RGD SPs (Figure 1d), indicating that these three components do participate in the composition of Fe_3O_4@PDA/VRL-RGD SPs. According to the standard curve of peak area versus concentration in HPLC (Figure S1), the loading rate and encapsulation rate of VRL in Fe_3O_4@PDA/VRL-RGD SPs are calculated as 15.3% and 18.0%, respectively, because VRL can only be loaded inside and on the surface of the PDA shell, but not in the Fe_3O_4 core. Therefore, the drug loading rate and encapsulation rate of VRL may not seem very high, but in fact, the content of VRL loaded in the PDA shell is very high.

With PDA coating, Fe_3O_4@PDA/VRL-RGD SPs exhibit high extinction ability at 808 nm with a molar extinction coefficient of the sample is 7.91 × 10^8 M^{-1} cm^{-1}, and can be used for photothermal therapy (Figure 1e). To investigate the photothermal properties of Fe_3O_4@PDA/VRL-RGD SPs in aqueous solutions, an 808 nm laser is used. Temperature increments increase with solution concentration when laser power density is fixed at 2 W/cm^2, due to the collective heating effect (Figure 2a). Further, the temperature increments increase with increasing laser power density at a fixed concentration of 200 μg/mL as more doses of exposure are applied (Figure 2b). Thermal imaging cameras are further used to monitor the process of heating, and the experimental data shows similar results as above (Figure S2). According to calculations, the photothermal conversion efficiency of Fe_3O_4@PDA/VRL-RGD SPs is 46.1% (Figure 2c,d). It should be noted here that in order to avoid the heat loss of solution caused by too long experiment time, we choose to conduct the experiment at a higher laser power density. However, this does not mean that low laser power density can not get higher heating effect. After avoiding heat loss through the insulation device (Figure S3a) as far as possible, the heating effect achieved after irradiation at 0.33 W/cm^2 for a long time is not weaker than 1 W/cm^2 (Figure S3b). NIR laser irradiation with a power density of 3 W/cm^2 is used to assess the photothermal stability of Fe_3O_4@PDA/VRL-RGD SPs. Despite 6 cycles of heating and cooling, the photothermal properties do not degrade (Figure 2e), and the absorption spectra slightly increased due to the evaporation of the solvent (Figure 2f).

The Fe_3O_4@PDA/VRL-RGD SPs are also magnetic because of the presence of Fe_3O_4 in the structure. Therefore, Fe_3O_4@PDA/VRL-RGD SPs dispersed in aqueous solution can be enriched under the action of magnetic field, which has the potential to be applied in magnetic targeted therapy (Figure S4). A circulating magnetic field between −30000 and +30000 Oe is used to measure the magnetic curve of the Fe_3O_4@PDA/VRL-RGD SPs. The saturation magnetization of Fe_3O_4@PDA/VRL-RGD SPs is 25.8 emu/g without any evident remanence or coercivity at 300 K. These results indicate that Fe_3O_4@PDA/VRL-RGD SPs are superparamagnetic and exhibit strong magnetism (Figure 3a). As a consequence, Fe_3O_4@PDA/VRL-RGD SPs can use as a good contrast agent for T_2-weighted MRI. A nuclear magnetic resonance (NMR) spectrometer is used to measure the transverse relaxation rate (r_2). As shown in Figure 3b, with the concentration of Fe_3O_4@

https://doi.org/10.1021/acsomega.2c07647
ACS Omega 2023, 8, 7891−7903

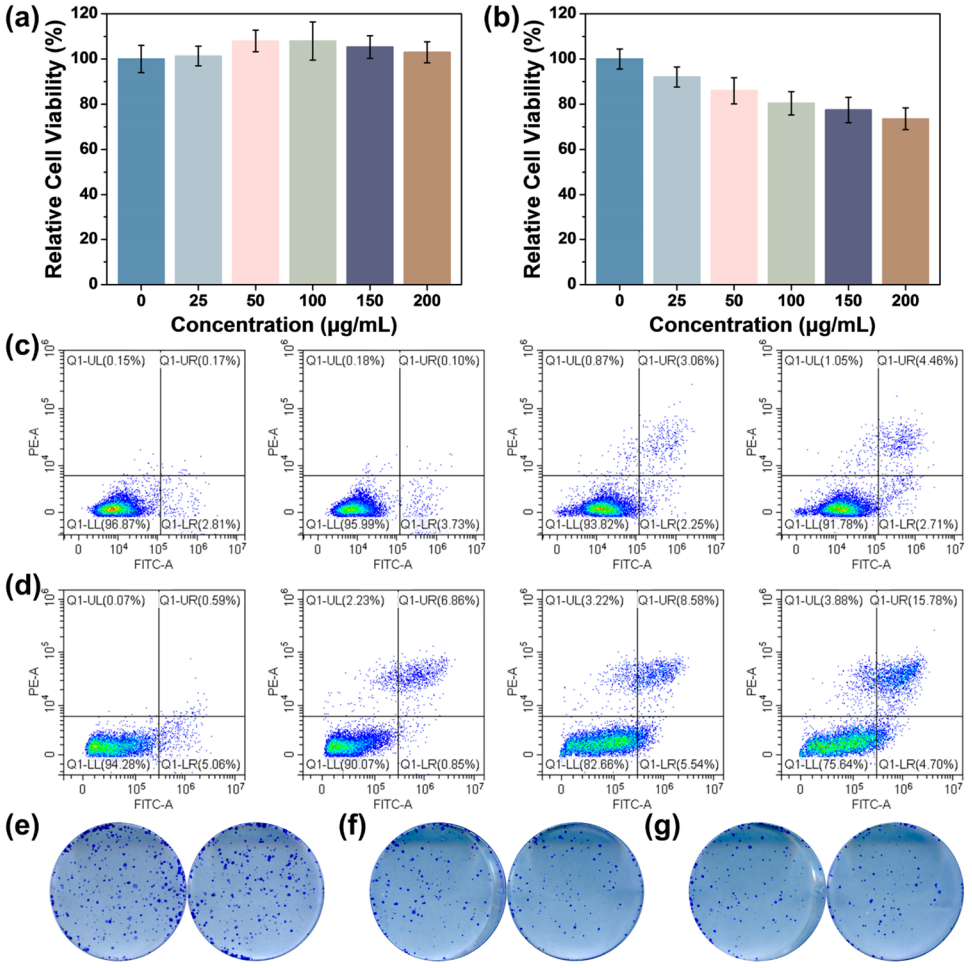

Figure 4. Ealy926 cells (a) and A549 cells (b) are incubated with Fe_3O_4@PDA/VRL-RGD SPs at different concentrations of 0, 25, 50, 100, 150, and 200 μg/mL for 24 h, and then, the relative cell viabilities are estimated through CCK-8 assay. (c) A549 cells were incubated with Fe_3O_4@PDA-RGD SPs at different concentrations of 0, 50, 100, and 200 μg/mL for 24 h, and then, the cell apoptosis are estimated through flow cytometry. (d) A549 cells were incubated with Fe_3O_4@PDA/VRL-RGD SPs at different concentrations of 0, 50, 100, and 200 μg/mL for 24 h, and then, the cell apoptosis are estimated through flow cytometry. A549 cells are incubated under normal conditions (e), with Fe_3O_4@PDA-RGD SPs at the concentration of 200 μg/mL for 2 h (f) and with Fe_3O_4@PDA/VRL-RGD SPs at the concentration of 200 μg/mL for 2 h (g), and then irradiated without (left) or with (right) 808 nm laser at 1 W/cm^2 for 10 min. The ability of colony formation is revealed by crystal violet staining.

PDA/VRL-RGD SPs increasing, the $1/T_2$ increases, and r_2 is calculated as 348.7 mM^{-1} s^{-1}. Additionally, as the concentration of Fe_3O_4@PDA/VRL-RGD SPs increases an increasing darkening effect is reflected in a 3.0 T MR clinical scanner (Figure S5). As a T_2-weighted MRI contrast agent, Fe_3O_4@PDA/VRL-RGD SPs could be useful for the diagnosis of tumors.

The zeta potential of Fe_3O_4@PDA/VRL-RGD SPs is −37.4 ± 0.6 mV. As a result of the negatively charged surface, Fe_3O_4@PDA/VRL-RGD SPs can disperse stably in aqueous solutions. Therefore, a further investigation of the colloidal stability of Fe_3O_4@PDA/VRL-RGD SPs reveals that they are stable and well dispersed in water, normal saline, PBS, cell culture medium, and cell culture medium containing 10% FBS during 7 days of incubation (Figure S6). It is worth noting that good colloidal stability is only applicable at the pH of physiological environment, while PDA shell can undergo structural disintegration in slightly acidic tumor microenvironment and release drugs to play the role of chemotherapy. The disintegration of PDA shell is also reflected in the weakening of extinction ability in the NIR region (Figure S7).

Under different conditions, HPLC is used to study the release behavior of VRL in Fe_3O_4@PDA/VRL-RGD SPs. As illustrated in Figure 3c, within 24 h, only 25.4% of VRL is released at pH 7.4 (physiological environment), whereas 47.3% of VRL is released from the Fe_3O_4@PDA/VRL-RGD SPs at pH 5.5 (tumor microenvironment). Then, NIR laser-triggered drug release is further studied. Also, in order to avoid heat loss affecting the experimental results, 1 W/cm^2 laser power density is selected. Prominently, due to the expansion of the PDA shell with heat, a rapid release of VRL from Fe_3O_4@PDA/VRL-RGD SPs is observed (Figure 3d). According to these results, both an acidic tumor microenvironment and a NIR laser play a role in the drug release process. In combination with the external application of the NIR laser, the acidic tumor microenvironment can stimulate the release of VRL when Fe_3O_4@PDA/VRL-RGD SPs are accumulated at the tumor site, minimizing the adverse reactions of VRL and achieving a good chemotherapy effect. Considering all the experiments above, it is evident that Fe_3O_4@PDA/VRL-RGD SPs possess excellent photothermal therapy, magnetic targeting, MRI imaging, and chemotherapy abilities.

https://doi.org/10.1021/acsomega.2c07647
ACS Omega 2023, 8, 7891−7903

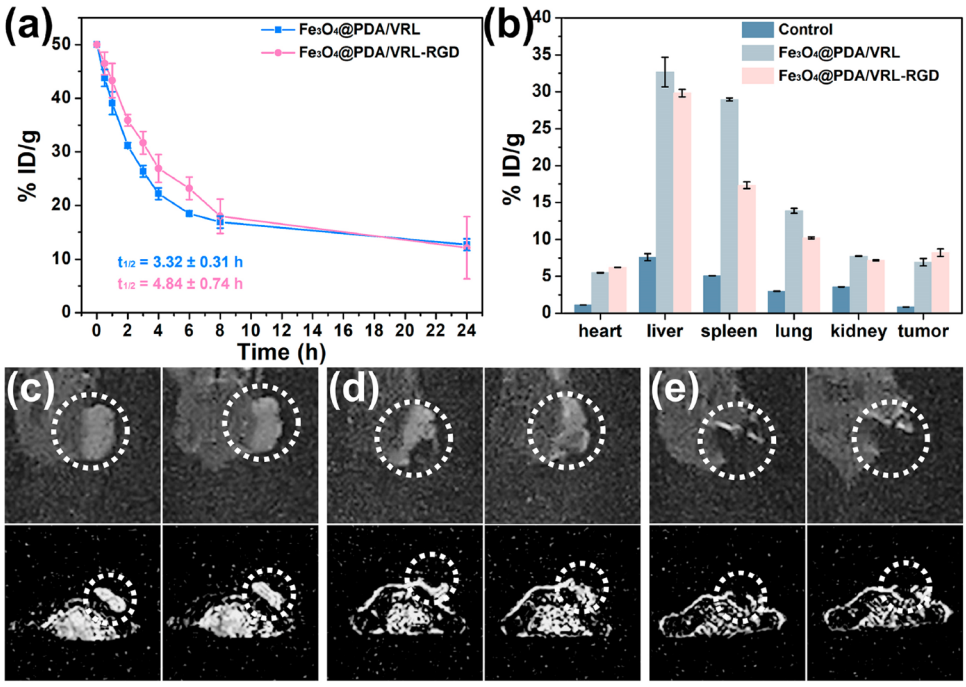

Figure 5. (a) Blood circulation of Fe_3O_4@PDA/VRL SPs and Fe_3O_4@PDA/VRL-RGD SPs *in vivo*. (b) Biodistribution of Fe_3O_4@PDA/VRL SPs and Fe_3O_4@PDA/VRL-RGD SPs in primary organs and tumors 24 h after the injection. Coronal and axial T_2-weighted MRI image of A549 tumor-bearing nude mice without treatment (c), 24 h after the injection of Fe_3O_4@PDA/VRL SPs (d), and 24 h after the injection of Fe_3O_4@PDA/VRL-RGD SPs (e).

In order to test the safety of Fe_3O_4@PDA/VRL-RGD SPs for biological applications *in vitro*, we first evaluate the cytotoxicity by using a cell counting kit-8 (CCK-8) assay. Ealy926 (human mesenteric artery vascular endothelial) cells are incubated with Fe_3O_4@PDA/VRL-RGD SPs at different concentrations (0−200 μg/mL) for 24 h. As shown in Figure 4a, the relative cell viability of Ealy926 cells is still ∼100% despite concentrations as high as 200 μg/mL, indicating that Fe_3O_4@PDA/VRL-RGD SPs do not have significant cytotoxicity to normal cells among the tested concentrations. This is because VRL works by stopping cell division in mitosis metaphase, the proliferation of normal cells is slow and the proportion of cells in the process of mitosis is low. Then, A549 cells are selected as the tumor cell model for the therapeutic experiments *in vitro*. The relative cell viability gradually decreases with the increased concentration of Fe_3O_4@PDA/VRL-RGD SPs. At a Fe_3O_4@PDA/VRL-RGD SPs concentration of 200 μg/mL, the relative cell viability is lower than 74% (Figure 4b). The toxicity of Fe_3O_4@PDA/VRL-RGD SPs to A549 cells is derived from the released VRL in tumor cells. And the increase of Fe_3O_4@PDA/VRL-RGD SPs concentration also increases the concentration of VRL cocultured A549 cells.

To verify this conclusion, the killing effect of Fe_3O_4@PDA-RGD SPs and Fe_3O_4@PDA/VRL-RGD SPs on A549 is compared by flow cytometry. A549 cells are cultured with Fe_3O_4@PDA-RGD SPs or Fe_3O_4@PDA/VRL-RGD SPs at different concentrations of 0, 50, 100, and 200 μg/mL for 24 h, then these cells are stained with annexin V-FITC and propidium iodide (PI) to investigate the apoptosis. As shown in Figure 4c, the percentages of viable cells decrease slightly attribute to the low toxicity and high biosafety of Fe_3O_4@PDA-RGD SPs without VRL. The cell viabilities are 96.87%, 95.99%, 93.82%, and 91.78%, respectively. As shown in Figure 4d, because of an increased release of chemotherapy drugs, the percentages of viable cells decrease gradually with increased concentrations of Fe_3O_4@PDA/VRL-RGD SPs. Significant differences exist among the viabilities of cells, which are 94.28%, 90.07%, 82.66%, and 75.64%, respectively. The results above demonstrate that chemotherapy of Fe_3O_4@PDA/VRL-RGD SPs is effective in killing A549 cells. However, single chemotherapy is not enough to kill tumor cells in large numbers, and NIR laser based photothermal therapy is further employed. At this moment, the heat production of nanoparticles dispersed in cell culture medium also faces the influence of heat loss under irradiation, so the laser power density is also set as 1 W/cm^2 in related tests. Photothermal therapy can not only directly improve the killing effect of tumor cells but also promote the release of chemotherapy drugs to achieve collaborative therapy. Though some cells are still alive after the chemotherapy and photothermal therapy combined, their proliferation ability is greatly diminished (Figure 4e−g). As compared to the control group, the Fe_3O_4@PDA/VRL-RGD SPs + laser group has a significantly lower clone formation rate of A549 cells (Figure 4e,g). The results of colony formation assay are further summarized into a statistical chart for intuitive observation (Figure S8). In summary, photothermal/chemotherapy is effective for ablating A549 cells. Even if some A549 cells can survive after collaborative treatment, their ability to proliferate is basically lost.

In animal experiments *in vivo*, first, the biosafety of Fe_3O_4@PDA/VRL-RGD SPs is systematically investigated. The relevant experiments are divided into three time points, and three evaluation methods are employed, respectively: Day 1: blood routine examination; Day 10: liver and renal function test; Day 20: histopathological analysis. One day after the Fe_3O_4@PDA/VRL-RGD SPs are injected into the mice through the tail vein, there is no obvious difference in the

https://doi.org/10.1021/acsomega.2c07647
ACS Omega 2023, 8, 7891−7903

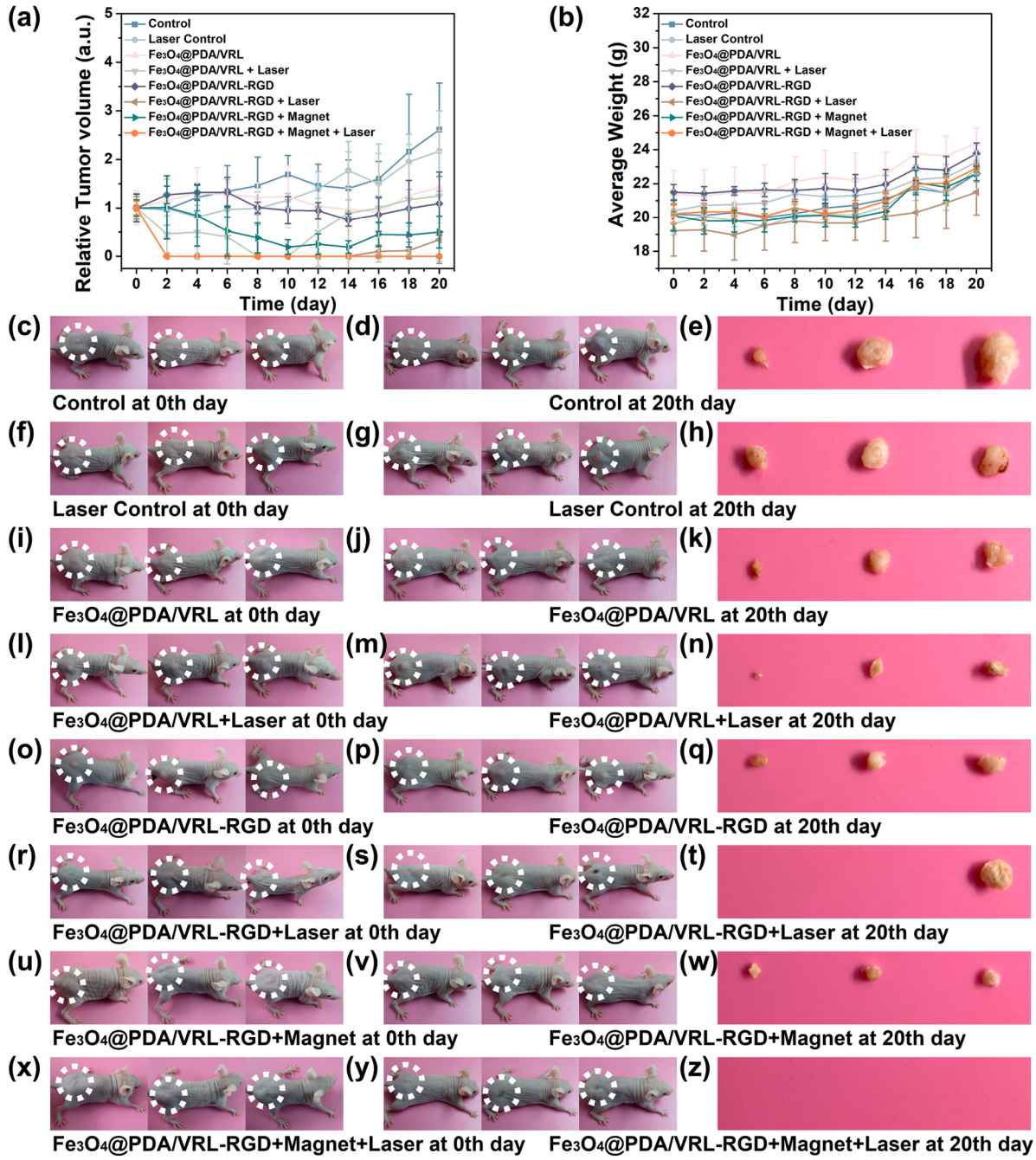

Figure 6. *In vivo* chemo-photothermal therapy. (a) Relative tumor volume curves for each group. (b) Average body weight curves for each group. Photographs of typical mice bearing A549 tumor before the treatment (c, f, i, l, o, r, u, x), after the treatment (d, g, j, m, p, s, v, y), and photographs of tumors after the treatment (e, h, k, n, q, t, w, z). The mice are divided into eight groups: (c–e) Control group, (f–h) Laser control group, (i–k) Fe_3O_4@PDA/VRL SPs group, (l–n) Fe_3O_4@PDA/VRL SPs + laser group, (o–q) Fe_3O_4@PDA/VRL-RGD SPs group, (r–t) Fe_3O_4@PDA/VRL-RGD SPs + laser group, (u–w) Fe_3O_4@PDA/VRL-RGD SPs + magnet group, and (x–z) Fe_3O_4@PDA/VRL-RGD SPs + magnet + laser group.

major blood routine examination between the experimental group and the control group of healthy mice with the same age (Figure S9), including white blood cell (WBC), red blood cell (RBC), mean corpuscular hemoglobin (MCH), hematokrit (HCT), lymphocyte (Lym), hemoglobin (HGB), mean platelet volume (MPV), and platelet (PLT). Ten days after the injection, the major liver function indexes, such as albumin (ALB), alkaline phosphatase (ALP), aspartate transaminase (AST), alanine aminotransferase (ALT), total protein (TP), and the major renal function indexes, such as UREA, uric acid (UA), and creatinine (CREA), between the control group and experimental group also show no significant difference (Figure S10). As shown in Figure S11, the H&E stained slices of vital organs from the experimental group on Day 20 do not show any significant pathological changes in comparison with those of the control group. These all confirm that Fe_3O_4@PDA/VRL-RGD SPs have good biosafety *in vivo*.

Then, the pharmacokinetic behavior is systematically studied. The content of Fe(III) in tumors, organs and blood samples is determined by ICP-AES. The half-life time of Fe_3O_4@PDA/VRL-RGD SPs and Fe_3O_4@PDA/VRL SPs in the blood is calculated as 4.84 ± 0.74 h and 3.32 ± 0.31 h

https://doi.org/10.1021/acsomega.2c07647
ACS Omega 2023, 8, 7891−7903

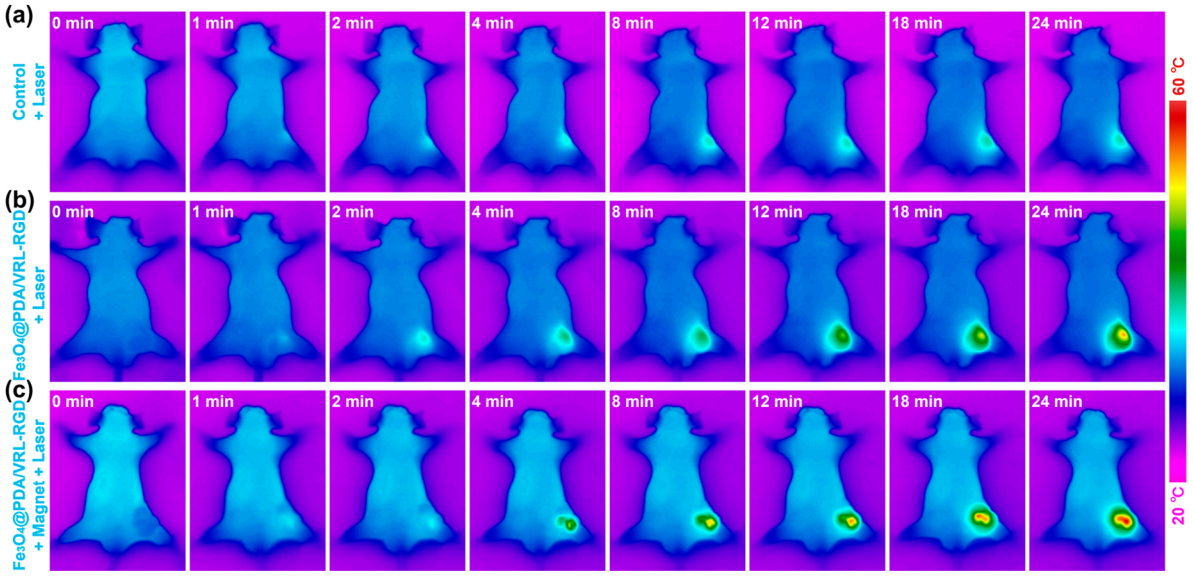

Figure 7. IR thermal images of A549 tumor bearing mice treated with saline + laser (a), Fe_3O_4@PDA/VRL-RGD SPs + laser (b), and Fe_3O_4@PDA/VRL-RGD SPs + magnet + laser (c), recorded by an IR camera. The laser power density is 0.33 W/cm^2, and the irradiation times are 0, 1, 2, 4, 8, 12, 18, and 24 min.

(Figure 5a). The prolonged blood circulation half-life is mainly attributed to the RGD targeting effect, which is beneficial for enhancing nanomaterials utilization and tumor enrichment. 24 h following injection, Fe_3O_4@PDA/VRL-RGD SPs attain a higher accumulation rate of 8.22 ± 0.51%ID/g at the tumor site under the action of EPR effect, as opposed to Fe_3O_4@PDA/VRL SPs which demonstrate a lower accumulation rate of 6.91 ± 0.50%ID/g (Figure 5b). In comparison with unmodified Fe_3O_4@PDA/VRL SPs, RGD-modified Fe_3O_4@PDA/VRL-RGD SPs exhibit enhanced targeting capabilities.

The enhanced tumor accumulation rate helps improve the diagnostic and therapeutic performance of Fe_3O_4@PDA/VRL-RGD SPs. An investigation of the diagnostic capability is conducted by T_2-weighted MRI. As shown in Figure 5c−e, mice injected with Fe_3O_4@PDA/VRL-RGD SPs have a higher accumulation rate, darker tumor sites, and clearer boundaries between tumors and surrounding normal tissues than mice injected with Fe_3O_4@PDA/VRL SPs, which is a reflection of RGD targeting capability. Consequently, Fe_3O_4@PDA/VRL-RGD SPs have an excellent ability to diagnose tumors. The tumor site in the control group shows bright gray, indicating a low signal on MRI. In these two experimental groups, the major organs are respectively dissected and dissolved with aqua regia in order to evaluate the biodistribution of nanomaterials. According to the calculation, the retention rate of Fe_3O_4@PDA/VRL SPs is 5.48 ± 0.03, 32.67 ± 2.00, 28.96 ± 0.19, 13.89 ± 0.33, and 7.73 ± 0.05%ID/g in the heart, liver, spleen, lung, and kidney, respectively. As compared to Fe_3O_4@PDA/VRL SPs, the retention rate of Fe_3O_4@PDA/VRL-RGD SPs reveals slightly decreased values, which is 6.21 ± 0.01, 29.82 ± 0.52, 17.34 ± 0.44, 10.21 ± 0.12, and 7.17 ± 0.07%ID/g, respectively, in these organs except heart (Figure 5b). There is no significant difference between the heart in these two experimental groups, which is considered to be caused by the residual amount of blood in the heart cavity. There is a significant enrichment of nanomaterials in the liver as a result of the phagocytosis of the reticuloendothelial system (RES), however, modification of the RGD produces a significant reduction in the number of enriched nanomaterials. The nonspecific retention of Fe_3O_4@PDA/VRL-RGD SPs in these major organs is minimized by RGD modification, which leads to low side effects *in vivo*.

Besides imaging diagnostics, photothermal therapy and chemotherapy are also possible with Fe_3O_4@PDA/VRL-RGD SPs. BALB/c nude mice are used as models of A549 tumors in the *in vivo* therapeutic studies. A control group of mice are injected only with normal saline, the tumors grow rapidly and the average volume reached 165.9 mm^3 20 days later (Figure 6a,c−e). The laser control group also shows similar results, with the average volume reaching 143.2 mm^3 after 20 days (Figure 6a,f−h). Accordingly, the laser alone is not effective in inhibiting tumor growth.

In the group of mice injected with Fe_3O_4@PDA/VRL SPs, there is a slight reduction in tumor growth rate and the average volume is 98.9 mm^3 (Figure 6a,i−k). The tumor microenvironment stimulates the release of VRL from nanomaterials, thereby inhibiting tumor growth. The average volume of tumors injected with Fe_3O_4@PDA/VRL-RGD SPs is 90.1 mm^3 and the tumor growth is also depressed (Figure 6a,o−q). In contrast to Fe_3O_4@PDA-VRL SPs, Fe_3O_4@PDA/VRL-RGD SPs are more concentrated in the tumor sites because of their specific binding between RGD and receptors on tumor cells. However, tumor growth is significantly inhibited by injection of Fe_3O_4@PDA/VRL-RGD SPs and attaching a magnetic targeting device (Figure S12), with an average volume of only 37.3 mm^3 (Figure 6a,u−w). It is due to the magnetic targeting ability of Fe_3O_4@PDA/VRL-RGD SPs under the action of the magnetic field, which further enhances the accumulation of nanomaterials in tumors. The tumor growth inhibition rates of groups (3), (5), and (7) are calculated as 45.5%, 58.3%, and 81.3%, respectively, on day 20 after injection.

However, tumor growth cannot be completely suppressed by chemotherapy alone. Thus, an 808 nm laser with the laser power density 0.33 W/cm^2, an FDA-approved biosafe power, is used to perform photothermal therapy to eliminate tumors. As shown in Figure 7, the temperature of the tumor site increases slowly in the laser control group, reaching 36.1 °C only after

https://doi.org/10.1021/acsomega.2c07647
ACS Omega 2023, 8, 7891−7903

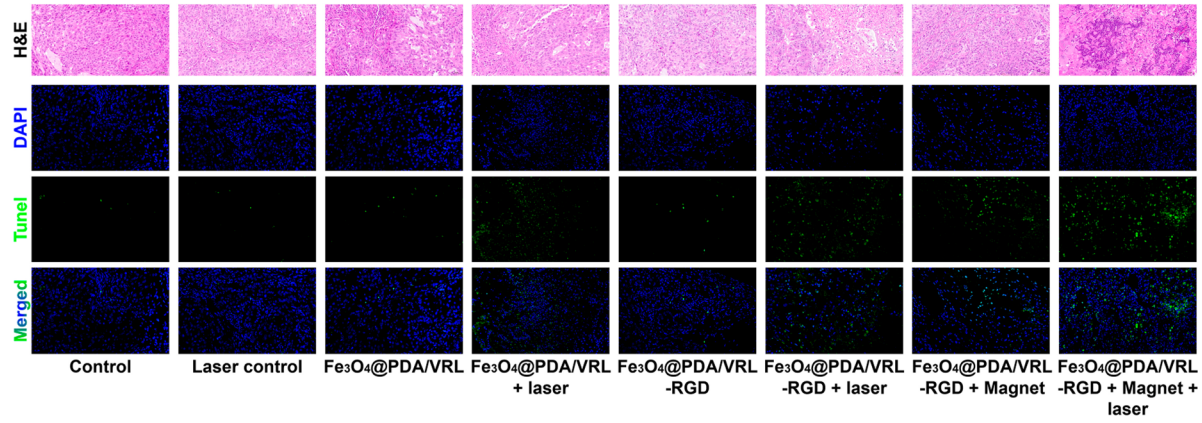

Figure 8. H&E and TUNEL stained tumor slices of each group (magnification: 200×).

24 min of irradiation. (Figure 7a). A significant improvement in heating performance is observed in mice treated with Fe_3O_4@PDA/VRL-RGD SPs and Fe_3O_4@PDA/VRL-RGD SPs + magnet in comparison to the control group. Infrared pictures reflect that the tumor site temperatures are 51.2 and 58.6 °C in these two groups after laser irradiation for 24 min (Figure 7b,c). Therefore, Fe_3O_4@PDA/VRL-RGD SPs with a magnetic field have a better photothermal therapy effect than those without, since more Fe_3O_4@PDA/VRL-RGD SPs are deposited in the tumor sites.

Following laser treatment, all groups of Fe_3O_4@PDA/VRL SPs + laser, Fe_3O_4@PDA/VRL-RGD SPs + laser, and Fe_3O_4@PDA/VRL-RGD SPs + magnet + laser show tumor ablation (Figure 6a,m,s,y). In the Fe_3O_4@PDA/VRL-RGD SPs + magnet + laser group, the tumors are completely ablated without recurrence (Figure 6a,x−z), but in the other two groups, tumor recurrences occur after 10 days (Figure 6a,l−n,r−t). Therefore, Fe_3O_4@PDA/VRL-RGD SPs can be accumulated efficiently in tumors under magnetic field conditions, allowing them to attain better therapeutic results with fewer nanomaterials, which has excellent future application potential. Additionally, in each group on day 20, average volumes and images of tumors show the effectiveness of the treatment. It is also important to note here that the 3 mice selected for photography have the largest, middle, and smallest tumor volume in each group, which we believe can more objectively and truly reflect the growth of tumors (Figure 6e,h,k,n,q,t,w,z). Across all groups, the weight of mice increases steadily, indicating that our treatment does not affect metabolism and is both safe and effective (Figure 6b).

H&E stained tumor slices show that the responsive release of superparticles-loaded chemotherapy drugs in the tumor microenvironment indeed kill tumor cells, even if the effect is limited. Photothermal therapy under NIR laser can kill tumor cells greatly and achieve tumor resection. The combination of chemotherapy and photothermal therapy shows a better treatment effect. Meanwhile, the higher the content of nanomaterials in the tumor, the better treatment effect, which is manifested by the increase of dead cells in H&E staining (Figure 8). TUNEL staining shows similar results: RGD/magnetic dual-targeting capability of superparticles significantly promotes apoptosis in tumor tissues (Figure 8), improves the synergistic therapeutic effect of photothermal/chemotherapy, and prevents tumor recurrence. Fe_3O_4@PDA/VRL-RGD SPs exhibits good performance in the theranostics of NSCLC.

CONCLUSIONS

In conclusion, we have successfully prepared Fe_3O_4@PDA/VRL-RGD SPs with the functions of MRI, photothermal therapy, and chemotherapy on NSCLC. The Fe_3O_4@PDA/VRL-RGD SPs have excellent therapeutic properties. As well as enhancing photothermal therapy abilities, the PDA shell reduces nanomaterials toxicity and enhances biocompatibility. Combined with the targeting effect of RGD, nanomaterials have a greater bioavailability. The half-life in the blood and tumor retention rate of the Fe_3O_4@PDA/VRL-RGD SPs are 4.84 ± 0.74 h and 8.22 ± 0.51%ID/g, respectively. Fe_3O_4@PDA/VRL-RGD SPs can be used in T_2-weighted MRI due to its super-paramagnetism. Applying a magnetic field to superparticles with magnetic targeting capabilities can further improve the diagnosis and therapeutic effects on tumors. Under the stimulation of the near-infrared laser and acidic tumor microenvironment, chemotherapeutic drugs can be released from the PDA shell for chemotherapy. On further combination with laser-induced photothermal therapy, NSCLC tumors can be effectively eliminated with no recurrence. Histopathology analysis of major organs and blood tests have confirmed the good biosafety profile of Fe_3O_4@PDA/VRL-RGD SPs. Our work provides a kind of nanomaterials with RGD/magnetic dual-targeting capability for MRI imaging and synergistic treatment of tumors through photothermal and chemotherapy, which has excellent application prospects in the future.

EXPERIMENTAL SECTION

Materials. Iron(III) acetylacetonate ($Fe(acac)_3$, 99.9+%), dopamine hydrochloride (DA), 1,2-hexadecanediol (90%), 1-octadecene (ODE, 90%), oleylamine (OLA, 70%), oleic acid (OA, 90%) were purchased from Sigma-Aldrich. Tris-(hydroxymethyl)aminomethane (Tris, 99.9+%), and vinorelbine ditartrate salt hydrate (VRL, 98+%) were purchased from Aladdin. Cyclo(Arg-Gly-Asp-D-Phe-Lys) RGD was purchased from Xi'an Ruixi Biomaterial Technology Co., Ltd. Sodium dodecyl sulfate (SDS) was purchased from Sinopharm Chemical Reagent Co., Ltd. Normal hexane, absolute ethanol, and toluene were of analytical grade. Cell culture medium (DMEM), trypsin digestion solution, cell counting kit-8 (CCK-8), and annexin V-FITC/PI apoptosis detection kit were bought from Solarbio. Fetal bovine serum (FBS) was bought from Biological Industries. Phosphate buffered solution (PBS), saline, and deionized water were used

https://doi.org/10.1021/acsomega.2c07647
ACS Omega 2023, 8, 7891−7903

as received. All reagents were used directly after the procurement and without any purification.

Preparation of Fe_3O_4 SPs. The thermal decomposition method was used to prepare Fe_3O_4 NPs with minor modifications from the previous method.[51] First, 2 mmol of $Fe(acac)_3$, 5 mmol of 1,2-hexadecanediol, 6 mmol of OA, and 6 mmol of OLA were mixed in 10 mL of ODE. After 15 min of stirring under a nitrogen atmosphere, the mixture was heated to 200 °C and maintained for 30 min. After the solution had been heated to 265 °C at a heating rate of 3 °C/min, it was refluxed for another 30 min at 265 °C. After the reaction, the solution was cooled to room temperature. The Fe_3O_4 NPs were dissolved in toluene after being extracted from the reaction solution and rinsed three times with absolute ethanol and normal hexane. An emulsification method was used to prepare Fe_3O_4 SPs. Under mechanical stirring at 400 rpm, 4 mL of methylbenzene solution of Fe_3O_4 NPs (7 mg/mL) was injected into SDS aqueous solution (4 mg/mL, 12.5 mL). After ultrasonication for 10 min, the emulsion was further heated in the water bath to 55 °C to evaporate toluene for 1.5 h to obtain Fe_3O_4 SPs.

Preparation of Fe_3O_4@PDA SPs and Fe_3O_4@PDA/VRL SPs. Fe_3O_4@PDA SPs were prepared based on our previous research.[52] First, 5 mL of 3 mg/mL Fe_3O_4 SPs aqueous solution was dispersed in 20 mL of Tris-buffer solution (10 mM, pH 8.5), then 1 mL of 5.6 mg/mL DA solution was added, and the mixture were stirred in the dark for 4.5 h at room temperature. After centrifuging at 8000 rpm for 15 min, Fe_3O_4@PDA SPs were gathered and finally washed three times with deionized water. As for the preparation of Fe_3O_4@PDA/VRL SPs, original DA solution was replaced with a mixture of DA and VRL (1 mL of 5.6 mg/mL DA and 1 mL of 10 mg/mL VRL).

Preparation of Fe_3O_4@PDA/VRL-RGD SPs. The as-perpared Fe_3O_4@PDA/VRL SPs were dispersed in 20 mL of Tris-buffer solution (10 mM, pH 8.5), and 1 mL of 5 mg/mL RGD aqueous solution was added. After stirring overnight in the dark at room temperature, deionized water was used to wash Fe_3O_4@PDA/VRL-RGD SPs three times after they were concentrated at 8000 rpm for 15 min. For further characterization, Fe_3O_4@PDA/VRL-RGD SPs were stored at 4 °C.

Photothermal, MRI, and Drug Release Functions *In Vitro*. In the exploration of photothermal property, 1.5 mL of Fe_3O_4@PDA/VRL-RGD SPs aqueous solution was added to a quartz pool. To prevent the vaporization of water, the quartz pool was covered with a tinfoil cap. A digital thermometer hanging above the light path was used to record the temperature of the solutions at an interval of 15 s. At the same time, an infrared thermal camera was also used to obtain infrared thermal images of the solutions. First, the Fe_3O_4@PDA/VRL-RGD SPs solutions at the concentrations of 0, 100, 200, and 300 μg/mL were irradiated by an 808 nm laser with a power density of 2 W/cm^2 until the temperature got stable. Second, the concentration of Fe_3O_4@PDA/VRL-RGD SPs solution was adjusted to 200 μg/mL, and the solution was irradiated by 808 nm laser with different power densities of 0, 1, 2, and 3 W/cm^2, respectively. Third, the Fe_3O_4@PDA/VRL-RGD SPs solution of 200 μg/mL was used for testing the photothermal conversion efficiency at 3 W/cm^2. Finally, the photothermal stability of Fe_3O_4@PDA/VRL-RGD SPs was observed by heating and cooling the solution for six cycles. The concentration of the solution was 1000 μg/mL, while the laser power density was 3 W/cm^2. In MRI tests *in vitro*, solutions of concentration-gradient Fe_3O_4@PDA/VRL-RGD SPs were prepared and their transverse relaxation time (T_2) were determined by NMR. Following this, T_2 was used to calculate the transverse relaxation rate (r_2) of Fe_3O_4@PDA/VRL-RGD SPs. To assess the MRI performance, Fe_3O_4@PDA/VRL-RGD SPs with different concentrations were determined by medical MRI instrument. The drug loading rate and encapsulation efficiency of VRL were investigated by HPLC. Drug Loading (%) = (WT − WF)/WNP × 100%. Encapsulation efficiency (%) = (WT − WF)/WT × 100%. WT is total weight of VRL fed. WF is the weight of nonencapsulated free VRL. WNP is the weight of nanoparticles. To investigate the drug release *in vitro*, PBS with a pH of 7.4 and 5.5 was used to dissolve Fe_3O_4@PDA/VRL-RGD SPs, respectively. Under different pH conditions, the release rates of chemotherapy drugs were compared, mainly including the contents of released VRL at 0, 0.5, 1, 2, 4, 8, and 24 h. Based on the above experiments, the solutions in each group were irradiated with near-infrared laser at 1 W/cm^2 for 5 min at minutes 5 and 15 to determine the effect of heat generated by Fe_3O_4@PDA/VRL-RGD SPs under near-infrared laser irradiation on drug release.

Cell Experiments *In Vitro*. As for cytotoxicity studies, Ealy926 and A549 cells were cultured with Fe_3O_4@PDA/VRL-RGD SPs at different concentrations. The relative viability of the cells was determined by CCK-8 assay after 24 h using the optical density at 450 nm. In order to investigate the killing effect of chemotherapy released by the responsive disintegration of PDA shell on tumor cells, flow cytometry was used to study the toxicity of Fe_3O_4@PDA-RGD SPs and Fe_3O_4@PDA/VRL-RGD SPs to A549 cells, respectively. A549 cells were cultured with Fe_3O_4@PDA-RGD SPs or Fe_3O_4@PDA/VRL-RGD SPs at different concentrations of 0, 50, 100, and 200 μg/mL, respectively. After 24 h, the cells were double-stained with PI and annexin-V-FITC and tested by flow cytometer to analyze cell apoptosis. In clonogenic assay, different conditions (Control, Fe_3O_4@PDA-RGD SPs at 200 μg/mL, and Fe_3O_4@PDA/VRL-RGD SPs at 200 μg/mL) were used to incubate A549 cells for 2 h and then irradiated with or without 808 nm laser at 1 W/cm^2 for 10 min. From the group above, 500 living cells were obtained, subsequently plated in 6-well plates, and cultured for several days. Meanwhile, cells were also observed every day to determine their growth status. In most single clones, a PBS wash was performed if the cell quantity exceeded 50, followed by paraformaldehyde fixation at 4%. Crystal violet was used to stain cells for 10 min after they had been washed twice with PBS. Finally, deionized water was used to wash the cells. A scanner was used to capture the photographs.

Safety *In Vivo*. Fifteen healthy BALB/c mice were intravenously (i.v.) injected with 50 μL of Fe_3O_4@PDA/VRL-RGD SPs (5 mg/mL). Then, 24 h after injection, the blood samples of five mice were collected for blood routine examination. Five mice were tested for liver and renal function 10 days after injection. Finally, 20 days after injection, the major organs of the other five mice were dissected, fixed with 10% formalin, and stained by H&E dye for further pathological examination. There were also another 15 healthy mice in the control group, and at each point, five of which were given the treatment as same as the experimental group.

Pharmacokinetic Performance and MRI Study *In Vivo*. The A549 tumor-bearing mice were i.v. injected with 50 μL of Fe_3O_4@PDA/VRL and Fe_3O_4@PDA/VRL-RGD SPs (5 mg/mL), respectively. Then, 6 μL of blood was collected from the

https://doi.org/10.1021/acsomega.2c07647
ACS Omega 2023, 8, 7891−7903

tail vein at 0, 0.5, 1, 2, 3, 4, 6, 8, and 24 h and dissolved in aqua regia for the ICP-AES test of Fe(III). After 24 h, the mice were anesthetized and imaged under a 3.0 T magnetic field to study their metabolism, especially in tumors. Again, after 24 h, the mice were euthanized and dissected. The major organs and tissues (liver, spleen, kidney, heart, lung, and tumor) were weighted and dissolved in aqua regia for the ICP-AES test of Fe(III).

Animal Experiments. All of the animal experiments related to this work were performed in accordance with the Guidelines for Care and Use of Laboratory Animals of Jilin University and approved by the Animal Ethics Committee of the First Hospital of Jilin University. From Beijing Vital River Laboratory Animal Technology Co., Ltd., 40 BALB/c nude mice (4-week-old, male) were purchased. To construct the NSCLC model, 150 μL of cell suspension containing 1.0×10^6 A549 cells was subcutaneously injected into the right buttocks of the mice. A549 tumor-bearing mice were randomly assigned to eight groups when the average tumor volume reached 50 mm^3: (1) Control group; (2) Laser control group; (3) Fe_3O_4@PDA/VRL SPs group; (4) Fe_3O_4@PDA/VRL SPs + laser group; (5) Fe_3O_4@PDA/VRL-RGD SPs group; (6) Fe_3O_4@PDA/VRL-RGD SPs + laser group; (7) Fe_3O_4@PDA/VRL-RGD SPs + magnet group; (8) Fe_3O_4@PDA/VRL-RGD SPs + magnet + laser group. In groups (1) and (2), 50 μL of normal saline was injected into mice. In groups (3) and (4), mice were i.v. injected with 50 μL of Fe_3O_4@PDA/VRL SPs (5 mg/mL). In groups (5)−(8), mice were i.v. injected with 50 μL of Fe_3O_4@PDA/VRL-RGD SPs (5 mg/mL). Meanwhile, the magnets were attached to the tumors of the mice of groups (7) and (8) for 24 h. The mice in groups (2), (4), (6), and (8) were treated with 0.33 W/cm^2 laser for 24 min. On a separate day, the tumor volumes ($V = 1/2LS^2$ mm^3, L represents the length of long axis and S represents the length of short axis) and weights (g) of the mice were recorded. The mice were photographed, euthanized, and dissected on day 20. After complete excision, tumors from each group were photographed and stained with H&E and TUNEL. Importantly, the three representative mice selected for photography have the largest, middle, and smallest tumor volumes in each group, which can more objectively and truly reflect the growth of tumors. As for groups (2), (4), (6), and (8), one tumor was excised immediately for histopathological examination after laser irradiation.

Characterization. TEM images were obtained by using an HT7800 transmission electron microscope (Hitachi, acceleration voltage: 120 kV). Fourier-transform infrared (FTIR) spectra were recorded using a VERTEX 80 V infrared spectrometer (Bruker). UV−vis−NIR absorption spectra were obtained by a UV3600 UV−vis−NIR spectrophotometer (Shimadzu). The zeta potential and hydrate particle size were determined using a Zetasizer NanoZS (Malvern). Flow cytometry analysis was performed by using a CytoFLEX (Beckman Coulter). The Fe concentrations was recorded by ICP-AES (Agilent 725). An investigation of magnetic property characterization was conducted by cycling a magnetic field between −30 and +30 kOe at 300 K using a SQUID magnetometer (QD MPMS). T_2 relaxation time was measured by an AVANCE III 500 MHz NMR spectroscope (Bruker). T_2-weighted MRI images were obtained by a 3.0T clinical MRI unit (uMR780, Shanghai United Imaging Healthcare Co., Ltd.). A TiR24 infrared thermal camera (Fluke) was used to acquire the thermal images. In the investigation of the photothermal effect, an 808 nm diode laser (LEO) was employed. High-pressure liquid chromatography (HPLC, Waters, Diamonsil C18 column (250 mm × 4.6 mm, 5 μm); mobile phase: methanol/5 mmol/L ammonium acetate = 65:35; detection speed: 0.2 mL/min; detection wavelength: 267 nm; column temperature: 20 °C; injection volume: 20 μL) was used to detect the drug loading rate, encapsulation rate, and drug release curve.

■ ASSOCIATED CONTENT

Supporting Information

The Supporting Information is available free of charge at https://pubs.acs.org/doi/10.1021/acsomega.2c07647.

Additional HPLC curve, thermal imaging photos, photos of solutions under magnetic field, T_2-weighted MRI images *in vitro*, photos of solutions in different solvents, UV absorption spectra, blood routine examination data, liver and renal function tests data, H&E stained primary organ slices and schematic illustration of the magnetic targeting device (PDF)

■ AUTHOR INFORMATION

Corresponding Authors

Shuwei Liu − *State Key Laboratory of Supramolecular Structure and Materials, College of Chemistry, Jilin University, Changchun 130012, P. R. China; Joint Laboratory of Optical Functional Theranostics in Medicine and Chemistry, The First Hospital of Jilin University, Changchun 130021, P. R. China;* orcid.org/0000-0002-9934-8183; Email: liushuwei@jlu.edu.cn

Hua Xin − *Department of Thoracic Surgery, China-Japan Union Hospital of Jilin University, Changchun 130031, P. R. China*; Email: xhua@jlu.edu.cn

Authors

Nan Zhao − *Department of Thoracic Surgery, China-Japan Union Hospital of Jilin University, Changchun 130031, P. R. China*

Qirui Sun − *State Key Laboratory of Supramolecular Structure and Materials, College of Chemistry, Jilin University, Changchun 130012, P. R. China*

Lening Zhang − *Department of Thoracic Surgery, China-Japan Union Hospital of Jilin University, Changchun 130031, P. R. China*

Hao Jin − *State Key Laboratory of Supramolecular Structure and Materials, College of Chemistry, Jilin University, Changchun 130012, P. R. China*

Mengsi Zhang − *State Key Laboratory of Supramolecular Structure and Materials, College of Chemistry, Jilin University, Changchun 130012, P. R. China*

Complete contact information is available at: https://pubs.acs.org/10.1021/acsomega.2c07647

Author Contributions

S.W.L. and H.X. proposed and supervised the project. N.Z. and S.W.L. designed the experiments. N.Z., Q.R.S., and L.N.Z. performed the experiments. N.Z., S.W.L., and H.X. cowrote the paper. H.J. and M.S.Z. participated in most experiments. All authors have given approval to the final version of the manuscript.

Notes

The authors declare no competing financial interest.

https://doi.org/10.1021/acsomega.2c07647
ACS Omega 2023, 8, 7891−7903

■ ACKNOWLEDGMENTS

This work was supported by the Science and Technology Development Program of Jilin Province (20210101230JC and YDZJ202201ZYTS055), the Science and Technology Project of Jilin Provincial Department of Education (JJKH20211199KJ and JJKH20221079KJ), the Project of Jilin Provincial Department of Finance (2021SCZ36), the Project funded by China Postdoctoral Science Foundation (2021TQ0125 and 2022M711303), the Interdisciplinary Integration and Innovation Project of Jilin University (JLUXKJC2021QZ10), and the Wu Jieping Medical Foundation (320.6750.2021-21-6).

■ REFERENCES

(1) Sung, H.; Ferlay, J.; Siegel, R. L.; Laversanne, M.; Soerjomataram, I.; Jemal, A.; Bray, F. Global cancer statistics 2020: GLOBOCAN estimates of incidence and mortality worldwide for 36 cancers in 185 countries. *CA-Cancer J. Clin.* **2021**, *71*, 209−249.
(2) Molina, J. R.; Yang, P. G.; Cassivi, S. D.; Schild, S. E.; Adjei, A. A. Non-small cell lung cancer: Epidemiology, risk factors, treatment, and survivorship. *Mayo Clin. Proc.* **2008**, *83*, 584−594.
(3) Sher, T.; Dy, G. K.; Adjei, A. A. Small cell lung cancer. *Mayo Clin. Proc.* **2008**, *83*, 355−367.
(4) Thai, A. A.; Solomon, B. J.; Sequist, L. V.; Gainor, J. F.; Heist, R. S. Lung cancer. *Lancet* **2021**, *398*, 535−554.
(5) Howington, J. A.; Blum, M. G.; Chang, A. C.; Balekian, A. A.; Murthy, S. C. Treatment of Stage I and II Non-small Cell Lung Cancer Diagnosis and Management of Lung Cancer, 3rd ed: American College of Chest Physicians Evidence-Based Clinical Practice Guidelines. *Chest* **2013**, *143*, e278S−e313S.
(6) Fidler-Benaoudia, M. M.; Torre, L. A.; Bray, F.; Ferlay, J.; Jemal, A. Lung cancer incidence in young women vs. young men: A systematic analysis in 40 countries. *Int. J. Cancer* **2020**, *147*, 811−819.
(7) Duma, N.; Santana-Davila, R.; Molina, J. R. Non-Small Cell Lung Cancer: Epidemiology, Screening, Diagnosis, and Treatment. *Mayo Clin. Proc.* **2019**, *94*, 1623−1640.
(8) Hirsch, F. R.; Scagliotti, G. V.; Mulshine, J. L.; Kwon, R.; Curran, W. J.; Wu, Y. L.; Paz-Ares, L. Lung cancer: current therapies and new targeted treatments. *Lancet* **2017**, *389*, 299−311.
(9) Oun, R.; Moussa, Y. E.; Wheate, N. J. The side effects of platinum-based chemotherapy drugs: a review for chemists. *Dalton Trans.* **2018**, *47*, 6645−6653.
(10) Sara, J. D.; Kaur, J.; Khodadadi, R.; Rehman, M.; Lobo, R.; Chakrabarti, S.; Herrmann, J.; Lerman, A.; Grothey, A. 5-fluorouracil and cardiotoxicity: a review. *Ther. Adv. Med. Oncol.* **2018**, *10*, 175883591878014.
(11) Pfister, C.; Gravis, G.; Flechon, A.; Soulie, M.; Guy, L.; Laguerre, B.; Mottet, N.; Joly, F.; Allory, Y.; Harter, V.; Culine, S. Randomized Phase III Trial of Dose-dense Methotrexate, Vinblastine, Doxorubicin, and Cisplatin, or Gemcitabine and Cisplatin as Perioperative Chemotherapy for Patients with Muscle-invasive Bladder Cancer. Analysis of the GETUG/AFU V05 VESPER Trial Secondary Endpoints: Chemotherapy Toxicity and Pathological Responses. *Eur. Urol.* **2021**, *79*, 214−221.
(12) Wolfram, J.; Ferrari, M. Clinical cancer nanomedicine. *Nano Today* **2019**, *25*, 85−98.
(13) Guo, X. J.; Cao, B.; Wang, C. Y.; Lu, S. Y.; Hu, X. L. In vivo photothermal inhibition of methicillin-resistant Staphylococcus aureus infection by in situ templated formulation of pathogen-targeting phototheranostics. *Nanoscale* **2020**, *12*, 7651−7659.
(14) Feng, L. L.; Gai, S. L.; He, F.; Yang, P. P.; Zhao, Y. L. Multifunctional Bismuth Ferrite Nanocatalysts with Optical and Magnetic Functions for Ultrasound-Enhanced Tumor Theranostics. *ACS Nano* **2020**, *14*, 7245−7258.
(15) Wang, C. Y.; Zhao, W.; Cao, B.; Wang, Z. X.; Zhou, Q.; Lu, S. Y.; Lu, L. G.; Zhan, M. X.; Hu, X. L. Biofilm-Responsive Polymeric Nanoparticles with Self-Adaptive Deep Penetration for In Vivo Photothermal Treatment of Implant Infection. *Chem. Mater.* **2020**, *32*, 7725−7738.
(16) Kalyane, D.; Raval, N.; Maheshwari, R.; Tambe, V.; Kalia, K.; Tekade, R. K. Employment of enhanced permeability and retention effect (EPR): Nanoparticle-based precision tools for targeting of therapeutic and diagnostic agent in cancer. *Mater. Sci. Eng., C* **2019**, *98*, 1252−1276.
(17) Sharma, P.; Mehta, M.; Dhanjal, D. S.; Kaur, S.; Gupta, G.; Singh, H.; Thangavelu, L.; Rajeshkumar, S.; Tambuwala, M.; Bakshi, H. A.; et al. Emerging trends in the novel drug delivery approaches for the treatment of lung cancer. *Chem.-Biol. Interact.* **2019**, *309*, 108720.
(18) Chen, H.; Zhang, W.; Zhu, G.; Xie, J.; Chen, X. Rethinking cancer nanotheranostics. *Nat. Rev. Mater.* **2017**, *2*, 17024.
(19) Li, T. Y.; He, F.; Liu, B.; Jia, T.; Shao, B. Y.; Zhao, R. X.; Zhu, H.; Yang, D.; Gai, S. L.; Yang, P. P. In Situ Synthesis of FeOCl in Hollow Dendritic Mesoporous Organosilicon for Ascorbic Acid-Enhanced and MR Imaging-Guided Chemodynamic Therapy in Neutral pH Conditions. *ACS Appl. Mater. Interfaces* **2020**, *12*, 56886−56897.
(20) Chen, B.; Dai, W.; He, B.; Zhang, H.; Wang, X.; Wang, Y.; Zhang, Q. Current Multistage Drug Delivery Systems Based on the Tumor Microenvironment. *Theranostics.* **2017**, *7*, 538−558.
(21) Dai, Y.; Xu, C.; Sun, X.; Chen, X. Nanoparticle design strategies for enhanced anticancer therapy by exploiting the tumour microenvironment. *Chem. Soc. Rev.* **2017**, *46*, 3830−3852.
(22) Ali, E. S.; Sharker, S. M.; Islam, M. T.; Khan, I. N.; Shaw, S.; Rahman, M. A.; Uddin, S. J.; Shill, M. C.; Rehman, S.; Das, N.; Ahmad, S.; Shilpi, J. A.; Tripathi, S.; Mishra, S. K.; Mubarak, M. S. Targeting cancer cells with nanotherapeutics and nanodiagnostics: Current status and future perspectives. *Semin. Cancer Biol.* **2021**, *69*, 52−68.
(23) Thakkar, S.; Sharma, D.; Kalia, K.; Tekade, R. K. Tumor microenvironment targeted nanotherapeutics for cancer therapy and diagnosis: A review. *Acta Biomater.* **2020**, *101*, 43−68.
(24) Sheikh, A.; Md, S.; Kesharwani, P. RGD engineered dendrimer nanotherapeutic as an emerging targeted approach in cancer therapy. *J. Controlled Release* **2021**, *340*, 221−242.
(25) Nieberler, M.; Reuning, U.; Reichart, F.; Notni, J.; Wester, H. J.; Schwaiger, M.; Weinmueller, M.; Raeder, A.; Steiger, K.; Kessler, H. Exploring the Role of RGD-Recognizing Integrins in Cancer. *Cancers* **2017**, *9*, 116.
(26) Danhier, F.; Le Breton, A.; Preat, V. RGD-Based Strategies To Target Alpha(v) Beta(3) Integrin in Cancer Therapy and Diagnosis. *Mol. Pharmaceutics* **2012**, *9*, 2961−2973.
(27) Huang, Z.-g.; Lv, F.-m.; Wang, J.; Cao, S.-j.; Liu, Z.-p.; Liu, Y.; Lu, W.-y. RGD-modified PEGylated paclitaxel nanocrystals with enhanced stability and tumor-targeting capability. *Int. J. Pharm.* **2019**, *556*, 217−225.
(28) Zhou, X.; Liu, H. Y.; Zhao, H.; Wang, T. RGD-modified nanoliposomes containing quercetin for lung cancer targeted treatment. *OncoTargets Ther.* **2018**, *11*, 5397−5405.
(29) Majumder, J.; Minko, T. Multifunctional and stimuli-responsive nanocarriers for targeted therapeutic delivery. *Expert Opin. Drug Delivery* **2021**, *18*, 205−227.
(30) Wang, Z. X.; Zhan, M. X.; Hu, X. L. Pulsed Laser Excited Photoacoustic Effect for Disease Diagnosis and Therapy. *Chem. - Eur. J.* **2022**, *28*, 202200042.
(31) Saadat, M.; Manshadi, M. K. D.; Mohammadi, M.; Zare, M. J.; Zarei, M.; Kamali, R.; Sanati-Nezhad, A. Magnetic particle targeting for diagnosis and therapy of lung cancers. *J. Controlled Release* **2020**, *328*, 776−791.
(32) Munaweera, I.; Shi, Y.; Koneru, B.; Saez, R.; Aliev, A.; Di Pasqua, A. J.; Balkus, K. J., Jr. Chemoradiotherapeutic Magnetic Nanoparticles for Targeted Treatment of Nonsmall Cell Lung Cancer. *Mol. Pharmaceutic* **2015**, *12*, 3588−3596.
(33) Al-Jamal, K. T.; Bai, J.; Wang, J. T. W.; Protti, A.; Southern, P.; Bogart, L.; Heidari, H.; Li, X. J.; Cakebread, A.; Asker, D.; Al-Jamal, W. T.; Shah, A.; Bals, S.; Sosabowski, J.; Pankhurst, Q. A. Magnetic

https://doi.org/10.1021/acsomega.2c07647
ACS Omega 2023, 8, 7891−7903

Drug Targeting: Preclinical in Vivo Studies, Mathematical Modeling, and Extrapolation to Humans. *Nano Lett.* **2016**, *16*, 5652−5660.
(34) Dadfar, S. M.; Roemhild, K.; Drude, N. I.; von Stillfried, S.; Knuchel, R.; Kiessling, F.; Lammers, T. Iron oxide nanoparticles: Diagnostic, therapeutic and theranostic applications. *Adv. Drug Delivery Rev.* **2019**, *138*, 302−325.
(35) Edis, Z.; Wang, J. L.; Waqas, M. K.; Ijaz, M.; Ijaz, M. Nanocarriers-Mediated Drug Delivery Systems for Anticancer Agents: An Overview and Perspectives. *Int. J. Nanomed.* **2021**, *16*, 1313−1330.
(36) Patra, J. K.; Das, G.; Fraceto, L. F.; Campos, E. V. R.; Rodriguez-Torres, M. D. P.; Acosta-Torres, L. S.; Diaz-Torres, L. A.; Grillo, R.; Swamy, M. K.; Sharma, S.; et al. Nano based drug delivery systems: recent developments and future prospects. *J. Nanobiotechnol.* **2018**, *16*, 71.
(37) He, J.; Huang, X. L.; Li, Y. C.; Liu, Y. J.; Babu, T.; Aronova, M. A.; Wang, S. J.; Lu, Z. Y.; Chen, X. Y.; Nie, Z. H. Self-Assembly of Amphiphilic Plasmonic Micelle-Like Nanoparticles in Selective Solvents. *J. Am. Chem. Soc.* **2013**, *135*, 7974−7984.
(38) Wu, M.; Zhang, D.; Zeng, Y. Y.; Wu, L. J.; Liu, X. L.; Liu, J. F. Nanocluster of superparamagnetic iron oxide nanoparticles coated with poly (dopamine) for magnetic field-targeting, highly sensitive MRI and photothermal cancer therapy. *Nanotechnology* **2015**, *26*, 115102.
(39) Xia, Y. S.; Tang, Z. Y. Monodisperse inorganic supraparticles: formation mechanism, properties and applications. *Chem. Commun.* **2012**, *48*, 6320−6336.
(40) Wang, Z.; Zou, Y.; Li, Y.; Cheng, Y. Metal-Containing Polydopamine Nanomaterials: Catalysis, Energy, and Theranostics. *Small* **2020**, *16*, 1907042.
(41) Bernsmann, F.; Ball, V.; Addiego, F.; Ponche, A.; Michel, M.; Gracio, J. J. D.; Toniazzo, V.; Ruch, D. Dopamine-Melanin Film Deposition Depends on the Used Oxidant and Buffer Solution. *Langmuir* **2011**, *27*, 2819−2825.
(42) Cheng, W.; Zeng, X.; Chen, H.; Li, Z.; Zeng, W.; Mei, L.; Zhao, Y. Versatile Polydopamine Platforms: Synthesis and Promising Applications for Surface Modification and Advanced Nanomedicine. *ACS Nano* **2019**, *13*, 8537−8565.
(43) Park, J.; Brust, T. F.; Lee, H. J.; Lee, S. C.; Watts, V. J.; Yeo, Y. Polydopamine-Based Simple and Versatile Surface Modification of Polymeric Nano Drug Carriers. *ACS Nano* **2014**, *8*, 3347−3356.
(44) Dong, Z. L.; Gong, H.; Gao, M.; Zhu, W. W.; Sun, X. Q.; Feng, L. Z.; Fu, T. T.; Li, Y. G.; Liu, Z. Polydopamine Nanoparticles as a Versatile Molecular Loading Platform to Enable Imaging-guided Cancer Combination Therapy. *Theranostics* **2016**, *6*, 1031−1042.
(45) Liu, Y.; Ai, K.; Liu, J.; Deng, M.; He, Y.; Lu, L. Dopamine-Melanin Colloidal Nanospheres: An Efficient Near-Infrared Photothermal Therapeutic Agent for In Vivo Cancer Therapy. *Adv. Mater.* **2013**, *25*, 1353−1359.
(46) Beik, J.; Abed, Z.; Ghoreishi, F. S.; Hosseini-Nami, S.; Mehrzadi, S.; Shakeri-Zadeh, A.; Kamrava, S. K. Nanotechnology in hyperthermia cancer therapy: From fundamental principles to advanced applications. *J. Controlled Release* **2016**, *235*, 205−221.
(47) Du, Y. Q.; Zhang, R.; Yang, J. N.; Liu, S. K.; Zhou, J. L.; Zhao, R. X.; He, F.; Zhang, Y. Q.; Yang, P. P.; Lin, J. A "Closed-Loop" Therapeutic Strategy Based on Mutually Reinforced Ferroptosis and Immunotherapy. *Adv. Funct. Mater.* **2022**, *32*, 2111784.
(48) Zhang, Y. B.; He, X.; Zhang, Y. T.; Zhao, Y. P.; Lu, S. Y.; Peng, Y. J.; Lu, L. G.; Hu, X. L.; Zhan, M. X. Native Mitochondria-Targeting polymeric nanoparticles for mild photothermal therapy rationally potentiated with immune checkpoints blockade to inhibit tumor recurrence and metastasis. *Chem. Eng. J.* **2021**, *424*, 130171.
(49) Chen, J. Q.; Ning, C. Y.; Zhou, Z. N.; Yu, P.; Zhu, Y.; Tan, G. X.; Mao, C. B. Nanomaterials as photothermal therapeutic agents. *Prog. Mater. Sci.* **2019**, *99*, 1−26.
(50) Chouly, C.; Pouliquen, D.; Lucet, I.; Jeune, J. J.; Jallet, P. Development of superparamagnetic nanoparticles for MRI: effect of particle size, charge and surface nature on biodistribution. *J. Microencapsulation* **1996**, *13*, 245−255.
(51) Sun, S. H.; Zeng, H. Size-controlled synthesis of magnetite nanoparticles. *J. Am. Chem. Soc.* **2002**, *124*, 8204−8205.
(52) Liu, S.-W.; Wang, L.; Lin, M.; Liu, Y.; Zhang, L.-N.; Zhang, H. Tumor Photothermal Therapy Employing Photothermal Inorganic Nanoparticles/Polymers Nanocomposites. *Chin. J. Polym. Sci.* **2019**, *37*, 115−128.

https://doi.org/10.1021/acsomega.2c07647
ACS Omega 2023, 8, 7891−7903